ARTICLE

Check for updates

Stabilizing indium sulfide for CO_2 electroreduction to formate at high rate by zinc incorporation

Li-Ping Chi [1,2], Zhuang-Zhuang Niu [1,2], Xiao-Long Zhang [1,2], Peng-Peng Yang [1], Jie Liao [1], Fei-Yue Gao [1], Zhi-Zheng Wu [1], Kai-Bin Tang [1✉] & Min-Rui Gao [1✉]

Recently developed solid-state catalysts can mediate carbon dioxide (CO_2) electroreduction to valuable products at high rates and selectivities. However, under commercially relevant current densities of >200 milliamperes per square centimeter (mA cm^{-2}), catalysts often undergo particle agglomeration, active-phase change, and/or element dissolution, making the long-term operational stability a considerable challenge. Here we report an indium sulfide catalyst that is stabilized by adding zinc in the structure and shows dramatically improved stability. The obtained $ZnIn_2S_4$ catalyst can reduce CO_2 to formate with 99.3% Faradaic efficiency at 300 mA cm^{-2} over 60 h of continuous operation without decay. By contrast, similarly synthesized indium sulfide without zinc participation deteriorates quickly under the same conditions. Combining experimental and theoretical studies, we unveil that the introduction of zinc largely enhances the covalency of In-S bonds, which "locks" sulfur—a catalytic site that can activate H_2O to react with CO_2, yielding HCOO* intermediates—from being dissolved during high-rate electrolysis.

---

[1] Division of Nanomaterials & Chemistry, Hefei National Laboratory for Physical Sciences at the Microscale, University of Science and Technology of China, Hefei 230026, China. [2] These authors contributed equally: Li-Ping Chi, Zhuang-Zhuang Niu, and Xiao-Long Zhang. ✉email: kbtang@ustc.edu.cn; mgao@ustc.edu.cn

Electrosynthesis of value-added fuels using carbon dioxide (CO_2) as a feedstock provides an appealing route to reduce climate-changing CO_2 emission and a solid stepping-stone towards carbon neutrality[1,2]. Over the past decade, the development of catalysts that are active and selective for CO_2 reduction reaction (CO_2RR), and meanwhile, suppress the competing hydrogen evolution, has been the subject of intensive study. This has resulted in a variety of carbon-based products to be synthesized from CO_2, such as carbon monoxide (CO)[3], formate ($HCOO^-$)[4], methane[5], and higher hydrocarbons and oxygenates (e.g., ethylene[6], ethanol[7], and n-propanol[8]). Despite remarkable advances, recent techno-economic analyses showed that CO and formate are probably the only products that can achieve the industrialization trend of CO_2RR in the near future[9,10]. Regarding the formate, its profitable production requires current densities of ≥ 200 mA cm^{-2}, Faradic efficiency (FE) of $> 90\%$, and power conversion efficiencies of $> 50\%$ (refs. [9,10]). Further, adopting solid-electrolyte electrolyzers permits the continuous production of formic acid without the separation process, making it even more economically viable[4].

Early research on CO_2RR from Hori and co-workers revealed that a number of metals, such as lead, mercury, indium (In), bismuth (Bi), cadmium, and tin, could convert CO_2 to formate, but many of these metals suffer from unsatisfactory selectivity or toxic issue[11]. Improvements in efficiency and selectivity have been achieved on nontoxic metallic catalysts via controlling of catalyst morphologies and dimensionalities[12,13], creation of vacancies[14], and introduction of other elements (e.g., O, S, and P) to form new phases[15–18]. When immobilized on the gas diffusion electrodes that surmount CO_2 mass transport limitation, commercially relevant rates (> 200 mA cm^{-2}) and FE ($> 90\%$) were observed to be reached on Bi nanosheets[19], Bi_2O_3 nanotubes[20], Bi metal-organic layers[21], and InP quantum dots[17]. However, the prospect on the potential of these catalysts for long-term operational stability is elusive. At high current densities, catalyst stability perhaps becomes a very important challenge. Often, CO_2RR activity deteriorates rapidly during high-rate electrolysis, owing to reasons like catalysis agglomeration[22], active-phase change[12,23], and element dissolution[15,24]. Unfortunately, previous research effort on catalyst stability, especially working at commercially relevant current densities, has remained rather rare. To make renewably powered formate electrosynthesis from CO_2 to be practical, it is critically necessary to develop catalysts that are not only active but also stable, and to gain insights on mechanisms of mediating the intrinsic stability.

Here, we report that incorporation of zinc (Zn) into indium sulfide (In_2S_3) synthesis enables tuning over its phase and structure, which dramatically improves the long-term stability of the resultant catalyst ($ZnIn_2S_4$) although the catalyst morphology remains almost unchanged. Comprehensive experiments coupled with computational studies reveal an enhanced covalency of In−S bonds mediated by Zn, which overstabilizes sulfur—a catalytic site that can activate H_2O to react with CO_2, leading to the formation of HCOO* intermediates—in the catalyst structure. Consequently, we achieved nearly 100% CO_2-to-formate conversion at a current density of 300 mA cm^{-2} over 60 h without degradation, corresponding to a high production rate of 8,894 µmol cm^{-2} h^{-1}.

Results

Synthesis and characterizations of catalysts. We had an interest in indium sulfide as a catalyst because S-doped In was shown by Wang and co-workers to be effective for catalyzing CO_2RR to formate. The presence of S enables facile activation of H_2O to form adsorbed H*, which consequently reacts with absorbed CO_2 to yield HCOO* intermediates[16]. However, the stability of S-doped In was only assessed under ~60 mA cm^{-2} during a 10 h period; the

prospect of such catalyst for durable high-rate CO_2-to-formate conversion is unclear. Very recently, Xia et al. reported that exfoliated ultrathin $ZnIn_2S_4$ nanosheets with rich Zn vacancies show improved CO_2RR ability to formate[14]. Although interesting, its long-term stability at current densities relevant to commercial operation (> 200 mA cm^{-2}) was not evaluated. These results motivated us to examine the ability of indium sulfide instead of S-doped In for mediating CO_2 to formate. We synthesized indium sulfide hydrothermally by the reaction of $InCl_3\cdot4H_2O$ and C_2H_5NS in deionized water (DIW) at 160 °C (Supplementary Fig. 1). Cubic In_2S_3 (JCPDS 65-0459; Fig. 1i) was produced after 6 h, exhibiting flower-like morphology composed of hierarchically organized nanosheets (Supplementary Fig. 2). Indeed, we observed good formate selectivity on In_2S_3, but the performance degraded quickly at high current densities owing to the dissolution of S^{2-} ions (discussion later).

Previous experimental studies revealed that adding Zn in some transition metal chalcogenides (e.g., Co_3S_4)[25] can enhance the structure robustness. Thus we sought to improve the stability of high-rate CO_2RR by incorporating Zn into indium sulfide. We used the same hydrothermal method for preparing the desired product except the addition of $ZnCl_2$ during the synthesis (Supplementary Fig. 1). Intriguingly, we obtained hexagonal-structured $ZnIn_2S_4$ (JCPDS 65-2023; Fig. 1i) microflowers that consist of hierarchically organized nanosheets (Fig. 1a, b), which closely resemble In_2S_3 described above. The thicknesses of nanosheets were determined to be ~8.69 nm for $ZnIn_2S_4$ and 9.32 nm for In_2S_3 through atomic force microscopy (AFM) measurements (Supplementary Fig. 3). We note that the synthesis of flower-like $ZnIn_2S_4$ was previously reported[26–28], whereas the analogous morphologies of $ZnIn_2S_4$ and In_2S_3 that synthesized by the same protocol here will underpin a fair performance comparison. Energy-dispersive X-ray (EDX) spectrum elemental mapping exhibits a uniform spatial distribution of Zn, In, and S (Fig. 1c). This simple synthetic strategy enables the production of high-yield $ZnIn_2S_4$ material with good fidelity for potential large-scale adoption (Supplementary Fig. 4).

We studied the detailed atomic structure of the $ZnIn_2S_4$ by high-angle annular dark-field scanning transmission electron microscopy (HAADF-STEM). The atomic-resolution Z-contrast images in Fig. 1d, e clearly reveal hexagonal lattice, where In atoms exhibit higher image intensity than the overlapped Zn and S atoms (Supplementary Fig. 5). The fast Fourier transform (FFT) result exhibits the (100) and (010) reflections (Fig. 1f). Using image contrast, the In and Zn(S) atoms can be further identified by the line intensity profile (Fig. 1g) acquired along the yellow arrow in Fig. 1d. The corresponding atomic model depicts that all the overlapped Zn and S atoms are located at the centers of honeycomb (Fig. 1h). Without the addition of Zn leads to the crystallization of cubic In_2S_3 by the same synthetic protocol (Fig. 1i and Supplementary Fig. 2). Structurally, $ZnIn_2S_4$ belongs to $(ZnS)_mIn_2S_3$ ($m = 1–3$) system[29], which bears an orderly alternation of S and Zn(In) (Fig. 1b, right). The sequence of atoms along the [001] direction is S−Zn_T−S−In_O−S−In_T−S, where Zn_T and In_T occupy the tetrahedral coordination and In_O occupies the octahedral site, respectively[29,30]. By comparison, one-third of the tetrahedral sites in In_2S_3 is unoccupied[31]. The incorporation of Zn alters the coordination environment of indium sulfide and thus might tailor favorably the electronic structure and catalytic properties.

To probe the electronic structures of $ZnIn_2S_4$ and In_2S_3, we measured the work function by ultraviolet photoelectron spectroscopy (UPS) (Fig. 1j). Our results show a lower work function of $ZnIn_2S_4$ (5.12 eV) compared to In_2S_3 (5.29 eV), revealing a superior electronic property by the incorporation of Zn element, consistent with electrochemical impedance spectroscopy (EIS) results (Supplementary Fig. 6). We speculate, on the basis of the
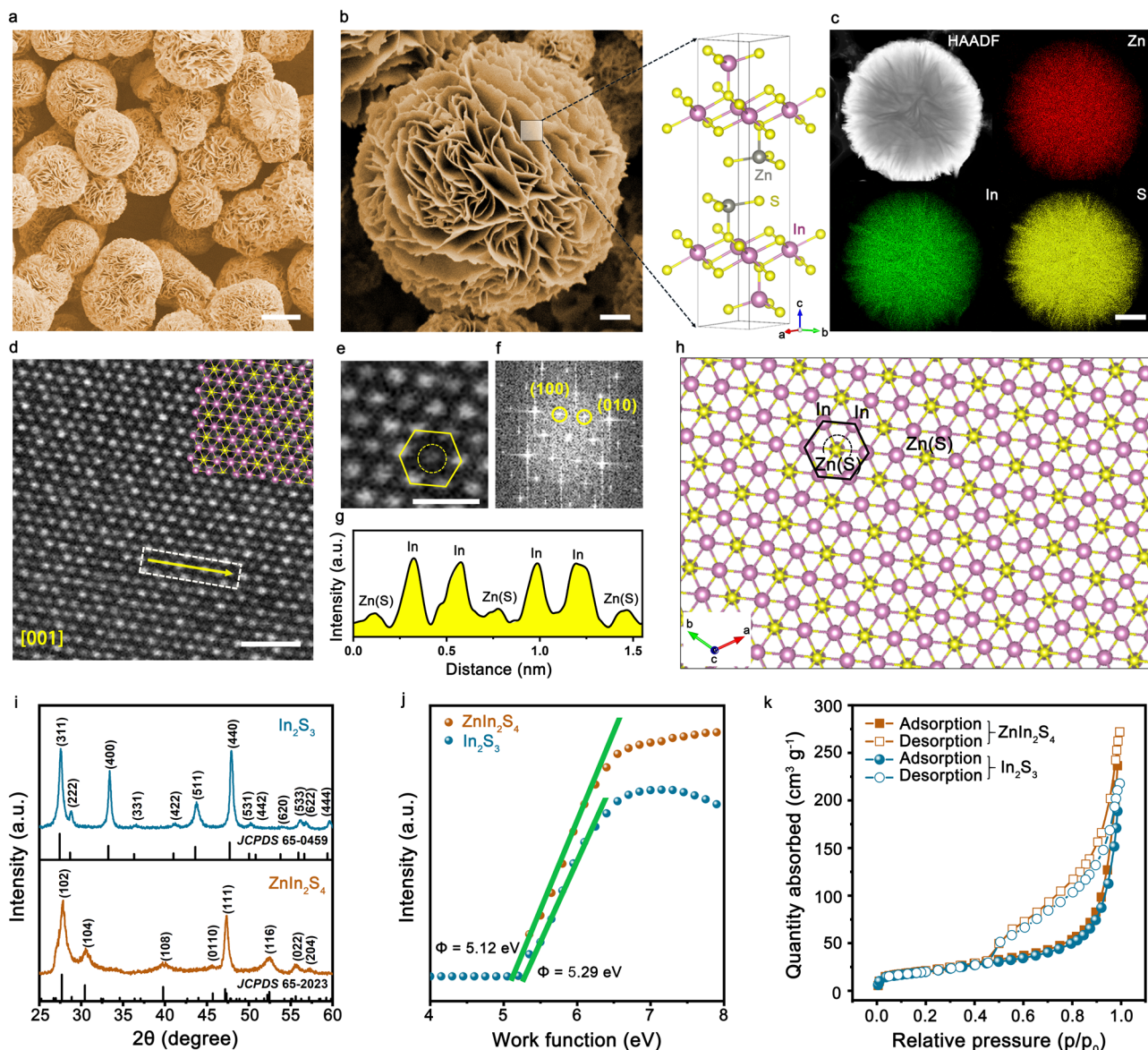
Fig. 1 Physical characterization of ZnIn₂S₄. a, b SEM images of the ZnIn₂S₄ catalyst. The right panel in **b** shows the crystal structure of ZnIn₂S₄. Scale bars, 5 μm (**a**) and 1 μm (**b**). **c** STEM-EDX elemental mapping of ZnIn₂S₄, exhibiting a uniform spatial distribution of Zn (red), In (green), and S (yellow), respectively. Scale bar, 1 μm. **d, e** Atomic-resolution Z-contrast images of ZnIn₂S₄ along [001] zone axis. Scale bars, 1 nm (**d**) and 0.5 nm (**e**). **f** The corresponding FFT pattern of (**d**). **g** The line intensity profile acquired along the yellow arrow in (**d**). **h** Atomic model of ZnIn₂S₄ along [001] zone axis. **i–k** XRD patterns (**i**), UPS spectra (**j**), and BET surface area analysis (**k**) of ZnIn₂S₄ and In₂S₃, respectively.

above results, that CO_2RR may be highly favored on such ternary In-based sulfide owing to the modulated coordination environment and electronic structure. Moreover, we determined the Brunauer–Emmett–Teller (BET) surface areas of $ZnIn_2S_4$ and In_2S_3 to be 71.3 and 70.0 m³ g⁻¹ (Fig. 1k), respectively.

CO_2RR performances in a flow cell. We examined CO_2RR properties of $ZnIn_2S_4$ and In_2S_3 catalysts in a flow cell (Supplementary Fig. 7) using recirculated 1 M $KHCO_3$ (pH 8.4) as electrolyte. CO_2 gas was fed at the cathode with a flow rate of 24 mL min⁻¹; the outlet gas flow rate was also measured for accurate product analysis (see "Methods"; Supplementary Fig. 8). We quantified the solution-phase and gas-phase products by using nuclear magnetic resonance (NMR) spectroscopy and on-line gas chromatography (Supplementary Fig. 9), respectively. The linear sweep voltammetry curves in Fig. 2a show sharp

reduction peaks for $ZnIn_2S_4$ and In_2S_3 catalysts in a CO_2 environment. In a N_2 environment, however, the two catalysts exhibit a slight current–voltage response. In comparison with In_2S_3, the onset potential for CO_2RR on $ZnIn_2S_4$ catalyst shifted to a more positive value, implying enhanced CO_2RR kinetics (Fig. 2a). Figure 2b shows that the Faradaic efficiency (FE) for formate on $ZnIn_2S_4$ catalyst was always greater than on In_2S_3 at all potentials examined (Supplementary Figs. 10, 11). Notably, the $ZnIn_2S_4$ catalyst yields peak FE of 99.3% for formate at −1.18 V versus a reversible hydrogen electrode (RHE), while the competing hydrogen evolution reaction (HER) on this catalyst was substantially suppressed (Fig. 2b and Supplementary Fig. 12). With this FE, we achieved a CO_2RR to formate partial current density of ~298 mA cm⁻² (Fig. 2c), representing the highest value reported to date under $KHCO_3$ environments (Fig. 2e). We also performed reference measurements of hexagonal ZnS (JCPDS 39-
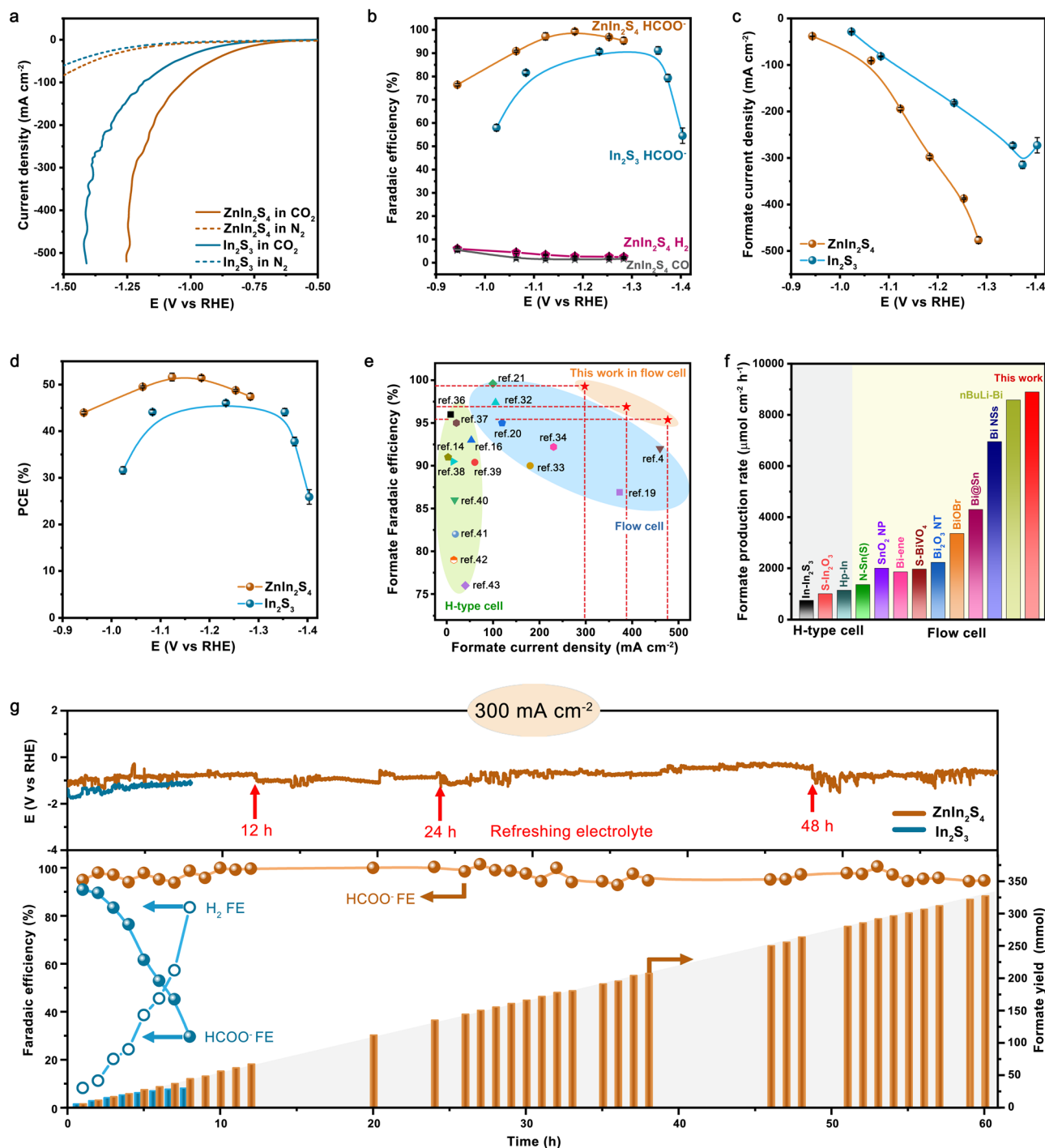
Fig. 2 CO$_2$RR performances. a, **b** The linear sweep voltammetry curves (**a**) and potential-dependent Faradaic efficiencies for products (**b**) on ZnIn$_2$S$_4$ and In$_2$S$_3$. **c**, **d** Partial current density (**c**) and half-cell PCE (**d**) for CO$_2$-to-formate conversion on ZnIn$_2$S$_4$ and In$_2$S$_3$. **e**, **f** Comparison of formate partial current densities and FEs (**e**), and formate production rates (**f**) for various catalysts reported under KHCO$_3$ environments (see Supplementary Table 1 for details). **g** Stability test of the ZnIn$_2$S$_4$ and In$_2$S$_3$ at 300 mA cm^{-2}. The electrolyte was occasionally replaced by new 1 M KHCO$_3$ solution (red arrows) to recover the ionic concentration and conductivity of the anolyte. The error bars represent the standard deviation of three independent measurements.

1363) that synthesized by the identical route for comparison, which, however, overwhelmingly produces H$_2$ (Supplementary Fig. 13). Additionally, our series of control experiments disclosed that the optimum CO$_2$RR performance was gained on ZnIn$_2$S$_4$ catalyst that hydrothermally synthesized at 160 °C for 6 h with a ZnCl$_2$:InCl$_3$·4H$_2$O ratio of 1:2 (Supplementary Figs. 14–19).

Figure 2d presents the half-cell power conversion efficiency (PCE) for CO$_2$-to-formate conversion under various applied

potentials. At −1.18 V versus RHE, our full-cell (CO$_2$ + H$_2$O → formate + O$_2$) device shows a half-cell formate PCE exceeding 50% on ZnIn$_2$S$_4$ catalyst. A comprehensive review of recent literature revealed that our ZnIn$_2$S$_4$ catalyst exhibits superb selectivity and partial current density (Fig. 2e), which result in a formate production rate of up to 8,894 μmol cm^{-2} h^{-1}, outperforming all previous results[4,14,16,19–21,24,32–43] that have been reported under KHCO$_3$ environments (Fig. 2f).

We used density functional theory (DFT) to obtain insights into the CO_2RR properties of the studied catalyst (see "Methods" for details). We compared the Gibbs free energies ($\triangle G$) for the formation of formate intermediate (HCOO*) on the surfaces of $ZnIn_2S_4$, In_2S_3, and In models (Supplementary Figs. 20–22). The computed barrier of HCOO* formation is 117 meV for $ZnIn_2S_4$ and 120 meV for In_2S_3, smaller than that of 270 meV for In, implying that S sites favorably mediate the HCOO* formation. Our calculations further reveal the lowest barrier of HCOOH* formation on $ZnIn_2S_4$, leading to its superior CO_2-to-formate ability. These results indicate that formate preferentially generates on $ZnIn_2S_4$ catalyst. By contrast, *COOH (intermediate of CO product) formation is highly endergonic on the three In-based catalysts (Supplementary Figs. 20–22), causing the production of CO to be virtually prohibited. Although HER process is largely hampered, our DFT results reveal that, as compared to In_2S_3 and In, the S sites of $ZnIn_2S_4$ enable much smaller hydrogen adsorption free energy of 370 meV. Early works[15,16] have reported that S acts as a promotor to enhance CO_2-to-formate conversion, we thus reasonably surmise that S sites on $ZnIn_2S_4$ surface permit easier H_2O dissociation to adsorbed H* species, which then react with CO_2 to yield HCOO* intermediates.

Comprehensive stability study. Aside from activity, long-term stability—especially operating at high current densities (> 200 mA cm^{-2})—is another critical metric for CO_2 electrolysis technique to be practical[10]. Figure 2g shows the key finding that we wish to report in this work: that is, the CO_2RR stability of indium sulfide can be remarkably improved by the incorporation of Zn. We tested the stability of $ZnIn_2S_4$ catalyst at a profitable current density as large as 300 mA cm^{-2}, during this process portions of the electrolyte were frequently taken out for NMR analysis. The formate FE could be held at > 97% over 60 h of continuous electrolysis without the need of additional overpotentials (Fig. 2g). By contrast, In_2S_3 reference exhibited a rapid drop in formate selectivity, whereas the FE toward H_2 climbed up to ~90% within 8 h. We hypothesize that such severe performance drop might be caused by the structure degradation during high-rate electrolysis. Notably, the exceptional stability of $ZnIn_2S_4$ catalyst enables us to produce ~327 mmol formate after 60 h (Fig. 2g).

We combined multiple characterization techniques to track the structural evolution of $ZnIn_2S_4$ and In_2S_3 catalysts during CO_2 electrolysis under various current densities and operating times (Fig. 3). X-ray diffraction (XRD) patterns and scanning electron microscopy (SEM) studies reveal that the phase and morphology of $ZnIn_2S_4$ catalyst were well retained when progressively increasing the current density even up to 500 mA cm^{-2} (Fig. 3a, c). By contrast, In_2S_3 catalyst undergoes a complete phase transition to metallic In (JCPDS 65-9292; Fig. 3b) at a current density of mere 50 mA cm^{-2}, accompanied by a dramatic morphology change (Fig. 3c, below images) owing to the loss of S that leads to structure collapse. Our Raman spectroscopy measurements on $ZnIn_2S_4$ show that two characteristic peaks at 248 (LO_1 mode) and 340 cm^{-1} (LO_2 mode)[44,45] were retained after 60 h of operation at 300 mA cm^{-2} (Fig. 3d). However, the characteristic Raman modes (A_{1g} and E_g)[46] of In_2S_3 disappeared while Raman signals from metallic In (ref. [47]) were detected within mere 1 min (Fig. 3e and Supplementary Figs. 23a, 24). The Raman results are consistent well with our post-mortem SEM analyses (Supplementary Fig. 25) and XRD results (Supplementary Fig. 23b).

Of note that the severe loss of S for In_2S_3 catalyst was further verified by X-ray photoelectron spectroscopy (XPS; Fig. 3g), STEM-EDX elemental mapping (Fig. 3h) and SEM-EDX (Fig. 3i). This is starkly contrasted with $ZnIn_2S_4$ whose chemical state and content of each elements (i.e., Zn, In, and S) were nearly unaltered after 60 h of high-rate CO_2 electrolysis

(Fig. 3f, h and Supplementary Figs. 26, 27). We quantified the amount of S remained in $ZnIn_2S_4$ and In_2S_3 catalysts by using SEM-EDX (Supplementary Figs. 28–30), which permits a quantitative compositional analysis at a relatively large scale. As shown in Fig. 3i, the amount of S in In_2S_3 drops to 2.13 wt% from its original value (23.6 wt%) within the first 1 h, followed by a slow drop to almost zero over the next 2 h. This result is consistent with the significantly increased S amount in an electrolyte that measured by inductively coupled plasma atomic emission spectroscopy (ICP-AES; Supplementary Fig. 31). By contrast, the $ZnIn_2S_4$ catalyst shows negligible loss of S after 60 h. Moreover, selected-area electron diffraction (SAED) analyses of the used $ZnIn_2S_4$ catalyst reveal that the single-crystalline hexagonal phase well maintains after the aggressive long-term stability test (Fig. 3j). We further note that ZnS catalyst also performs very stable at high current densities (Supplementary Fig. 32) owing to the strong interaction between Zn and S (refs. [16,48,49]), although it mainly produces H_2 (Supplementary Fig. 13).

Stability enhancement mechanism. Our results above conclusively demonstrate that the stability degradation of In_2S_3 can be attributable to S leaching, and show the primacy of Zn as a stabilizer in indium sulfide that prevents S to be leached out. Besides indium sulfide, S leaching was also widely observed in other metal sulfides, while the dissolution mechanism is rather complex[6,18,50,51]. We turned to use DFT calculations to study the cause of the enhanced stability of indium sulfide after incorporating Zn. Compared with In_2S_3 having tetrahedral vacancies[31], the tetrahedral and octahedral sites in $ZnIn_2S_4$ are fully occupied[30] after Zn incorporation. Notably, in $ZnIn_2S_4$, all Zn atoms bind with S through tetrahedral coordination, which implies the formation of strong Zn_T−S bonds considering that tetrahedral structures commonly give covalent feature[52]. Our computed differential charge density and its projection on the (110) plane map clearly reveal an enhanced electron cloud between Zn and S atoms (Fig. 4a, b), revealing electron donation from Zn to S due to the strong reducibility of Zn atoms. The transfer of electrons from In to S can also be seen more pronounced in $ZnIn_2S_4$ (Fig. 4a, b) than that in In_2S_3 (Fig. 4d, e), which leads to charge accumulation around In−S bonds and correspondingly higher covalency[53].

The calculated electronic localization function (ELF) of the tetrahedral In_T−S and octahedral In_O−S bonds in $ZnIn_2S_4$ are 0.84 and 0.79 (Fig. 4c), which compare larger than that of 0.71 and 0.76 in In_2S_3 (Fig. 4f), indicating a greater localization of S−In_O−S−In_T−S (ref. [54]). Likewise, the ELF of tetrahedral Zn_T−S bond in $ZnIn_2S_4$ was calculated to be 0.81 (Fig. 4c), pointing to its localized covalent feature. The interatomic bond strengths were further quantitatively analyzed by the projected crystal orbital Hamilton population (pCOHP) method (Fig. 4g−i). We found that the anti-bonding orbitals of In−S and Zn−S for $ZnIn_2S_4$ are less occupied. Moreover, our calculations yield integrated pCOHP values below the Fermi level of −0.763 and −0.737 for In−S bonds in $ZnIn_2S_4$ and In_2S_3, respectively, again demonstrating greater bond strengths in $ZnIn_2S_4$ (ref. [55]). These results, therefore, indicate that the bond breaking between In(Zn) and S in $ZnIn_2S_4$ is kinetically cumbersome, which explains the negligible S dissolution and thus exceptional long-term stability of the $ZnIn_2S_4$ catalyst (Supplementary Fig. 33).

Discussion

In closing, we have shown long-term formate electrosynthesis from CO_2 at a high current density of 300 mA cm^{-2} on a cost-effective
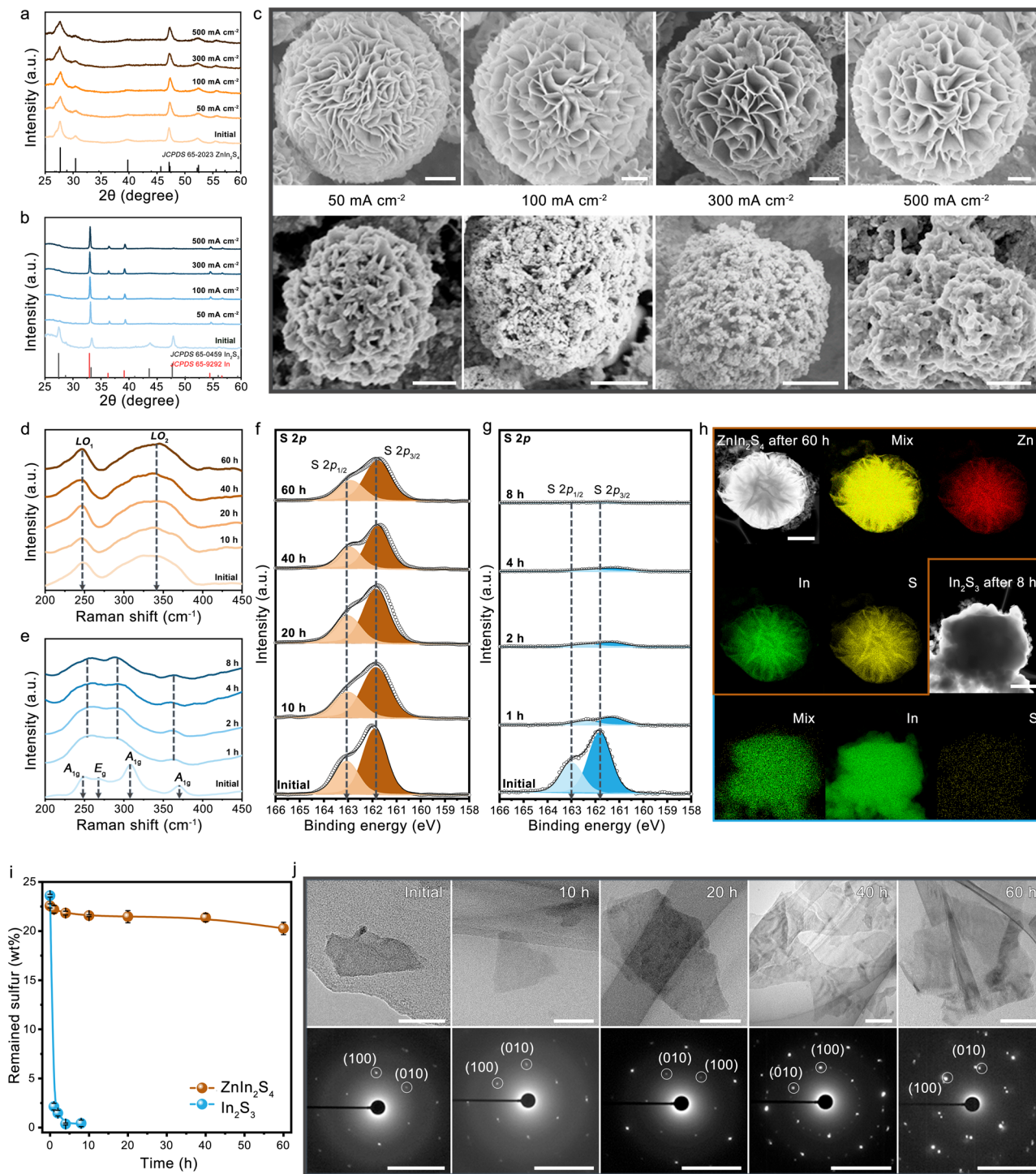
Fig. 3 Structural stability of ZnIn$_2$S$_4$. a, b XRD patterns of ZnIn$_2$S$_4$ (**a**) and In$_2$S$_3$ (**b**) after CO$_2$ /Subscript> electrolysis under various current densities for 10 min. **c** Corresponding SEM images of ZnIn$_2$S$_4$ (above) and In$_2$S$_3$ (bottom). Scale bars, 1 μm (above) and 500 nm (bottom). **d–g** Raman spectra of ZnIn$_2$S$_4$ (**d**) and In$_2$S$_3$ (**e**), and S 2p XPS spectra of ZnIn$_2$S$_4$ (**f**) and In$_2$S$_3$ (**g**) after CO$_2$ electrolysis for various times at 300 mA cm^{-2}. **h** STEM-EDX elemental mappings of ZnIn$_2$S$_4$ (scale bar: 1 μm) and In$_2$S$_3$ (scale bar: 600 nm) after running for 60 h and 8 h at 300 mA cm^{-2}, respectively. **i** SEM-EDX measurements of the remained sulfur in catalysts after running for various times at 300 mA cm^{-2}. The error bars represent the standard deviation of three independent measurements. **j** TEM (above, scale bars: 50 nm) and SAED patterns (down, scale bars: 5 1/nm) of ZnIn$_2$S$_4$ catalyst after CO$_2$ electrolysis for various times at 300 mA cm^{-2}.

indium sulfide catalyst modulated by Zn. The extraordinary catalyst stability can be explained by the increase of In−S covalency, which substantially prevents sulfur dissolution during CO$_2$RR. We achieved selective and fast CO$_2$-to-formate conversion with a formate FE of 99.3% and a notable formate production rate of 8,894 μmol cm^{-2} h^{-1}. These findings will advance the development

of efficient and durable catalysts for commercial-scale electro-synthesis of formate.

Methods

Material synthesis. All chemicals were used as received without further purifica-tion. Indium chloride tetrahydrate (InCl$_3$·4H$_2$O), thioacetamide (C$_2$H$_5$NS), and Zinc

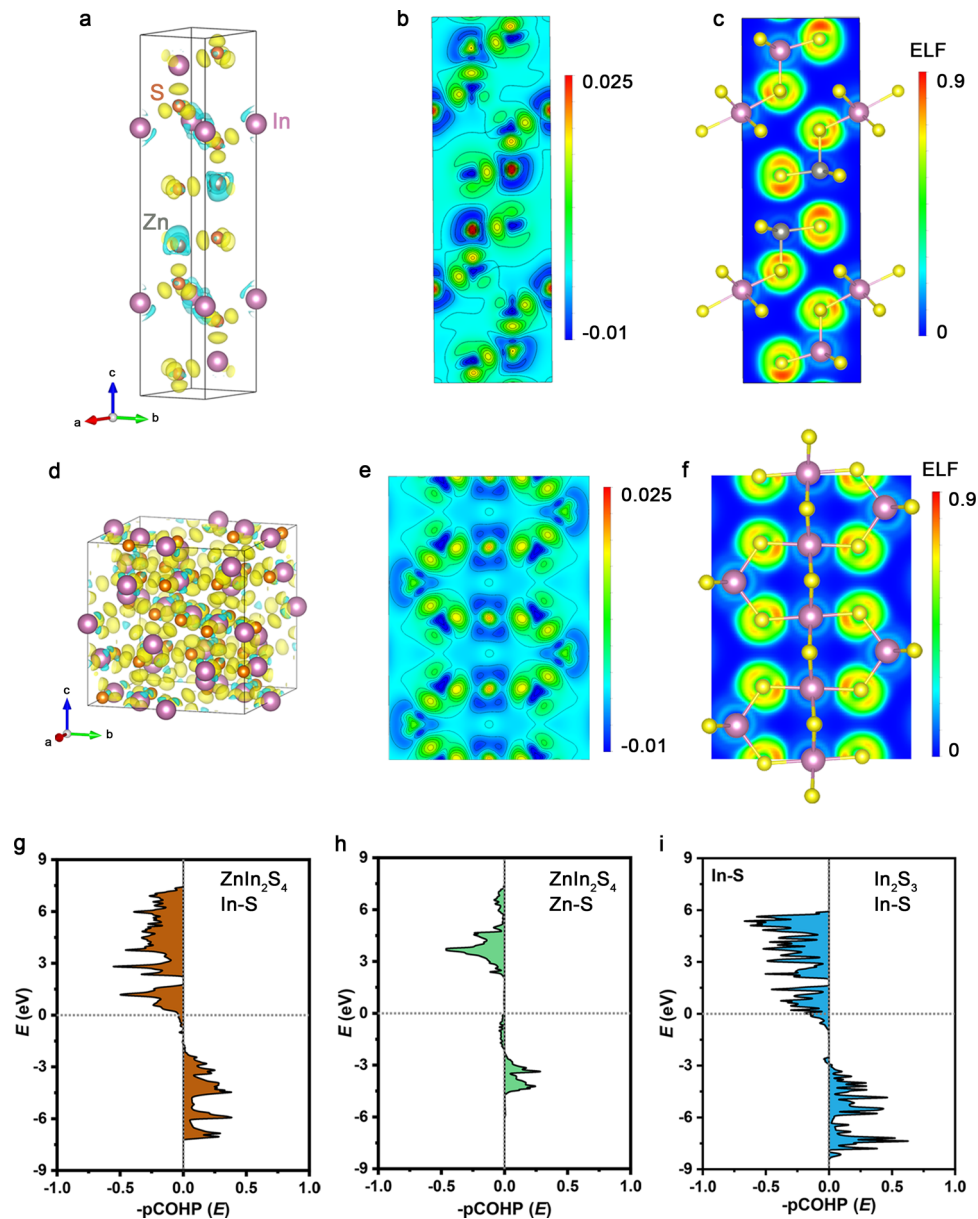**Fig. 4 Enhanced covalency in ZnIn₂S₄.** **a**, **b** Differential charge density (**a**) and projection on the (110) plane (**b**). **c** ELF of ZnIn₂S₄. **d**, **e** Differential charge density (**d**) and projection on the (011) plane (**e**). **f** ELF of In₂S₃. The azure and yellow clouds represent electron density depressions and accumulations, respectively. **g–i** COHPs for In−S bonding (**g**) and Zn−S bonding (**h**) of ZnIn₂S₄, as well as In−S bonding (**i**) of In₂S₃.

dichloride (ZnCl₂), were purchased from Sinopharm Chemical Reagent Co., Ltd (Shanghai, China). In a typical experiment, 3.0 mmol InCl₃·4H₂O was dissolved in 150 mL deionized water (DIW), and then 6.1 mmol C₂H₅NS was added with vigorous stirring for 20 min. The 20 mL resultant solution was transferred into a 50 mL Teflon-lined autoclave, sealed, and heated at 160 °C for 6 h. After the reaction, the obtained In₂S₃ powders were washed with excess DIW and absolute ethanol for at least three times, and then dried at room temperature in an oven under vacuum for further characterization. The synthesis of ZnIn₂S₄ was the same with the synthesis of In₂S₃, except the addition of 1.5 mmol ZnCl₂ during the first step. For the synthesis of ZnS, it needs to replace 3.0 mmol InCl₃·4H₂O with 1.5 mmol ZnCl₂.

Material characterizations. XRD was performed on a Japan Rigaku DMax-γA X-ray diffractometer with Cu Kα radiation (λ = 1.54178 Å). The morphology of the samples was investigated by SEM (Zersss Supra 40) and TEM (JEOL 2010F(s)). The STEM and HRTEM images, SAED and EDX elemental mapping were taken on JEMARM 200 F Atomic Resolution Analytical Microscope with an acceleration voltage of 200 kV. SEM-EDX was determined by GeminiSEM 500 with an Oxford Aztec series X-ray energy spectrum. Raman spectra was measured on a Raman microscope (HORIBA) with a 785 nm excitation laser. ICP-AES data were obtained by an Optima 7300 DV instrument. N₂ adsorption/

desorption isotherms were recorded on an ASAP 2020 accelerated surface area and a porosimetry instrument (Mictromeritics), equipped with an automated surface area, at 77 K by using Barrett−Emmett−Teller calculations. XPS was taken on an X-ray photoelectron spectrometer (ESCALab MKII) with an X-ray source (Mg Kα $h\upsilon = 1253.6$ eV).

Preparation of CO₂RR electrodes. The catalyst ink was prepared by ultrasonic dispersion of 10 mg catalyst powders in 1 ml isopropanol, which was mixed with 50 μL of 5 wt% Nafion. The resulted ink was uniformly spread on the gas diffusion layer (GDL, Sigracet 29 BC) of 3 × 3 cm² in the area by using an airbrush, yielding the prepared electrode with a catalyst loading of ~1.0 mg cm⁻².

Electrochemical measurements. All electrochemical measurements were performed in a flow cell with VSP-300 Potentiostat (Bio-Logic, France). For experiments in flow cells, gaseous CO₂ (99.999%) was passed through the gas chamber at the back side of the gas diffusion electrodes. Both catholyte and anolyte (1 M KHCO₃) were continuously circulated through the cathode and anode chambers separated by the cation exchange membrane (Nafion™ 117), which was used to avoid the crossover issues of formate[56]. The cathode is the prepared gas diffusion electrode (GDE, 1 × 1 cm²), and the anode is a piece of nickel foam (1 × 1 cm²).

The CO_2 inlet flowrates were kept constant at 24 mL min^{-1} by a mass flow controller (C100L, Sierra). $KHCO_3$ electrolyte flowrates were maintained constant at 20 mL min^{-1} controlled by a peristaltic pump (BT100-2J, Longer Pump). The CO_2 electrolysis lasted for 10 min unless otherwise specified. The linear sweep voltammetry (LSV) curves of $ZnIn_2S_4$ and In_2S_3 were performed in CO_2-fed and Ar-fed 1 M $KHCO_3$ solution. All potentials were measured against an Ag/AgCl (saturated KCl) reference electrode and converted to the RHE reference scale with iR correction on account of the equation:

$$E\,(\text{vs RHE}) = E\,(\text{vs Ag/AgCl}) + 0.205 + (0.0591 \times \text{pH}) - iR_s \tag{1}$$

Where the solution resistance R_s was determined by EIS over a frequency range from 100 KHz to 10 mHz.

CO_2RR products analysis. The gas products were analyzed by gas chromatography (GC-2014, Shimadzu) equipped with thermal conductivity detector (TCD) to quantify H_2 concentration and flame ionization detector (FID) to analyze the content of CO. Considering CO_2 consumption, the outlet flow rate was monitored by a mass flowmeter (AST10-HLC, Asert Instruments) before flowing to the on-line GC. The Faradaic efficiency for gas products (FE_x) was calculated by the following formula:

$$FE_x(\%) = \frac{n_x \times C_x \times u \times F}{I \times V_M} \times 100\% \tag{2}$$

where F is the Faraday constant (96485 C mol^{-1}), I is the total current density, n_x is electrons transferred for reduction to product x, C_x is volume fraction of the product x detected by GC, u is outlet gas flowrate and V_M is molar volume (22.4 L mol^{-1}).

The formate products were quantified by ^{1}H NMR spectra measured with a Bruker 400 MHz spectrometer. Typically, 400 μL of the electrolyte after CO_2RR electrolysis was mixed with 200 μL of D_2O containing 50 ppm (m/m) dimethyl sulphoxide (DMSO) as the internal standard. The area ratio of the formate peak to the DMSO peak was compared to the standard curve to quantify the concentration of formate. The molar quantity of formate ($n_{formate}$) was calculated via multiplying the concentration of formate with the volume of the catholyte. The Faradaic efficiency of the formate ($FE_{formate}$) can be calculated by the following equation:

$$FE_{formate}(\%) = 2 \times F \times \frac{n_{formate}}{I \times t} \times 100\% \tag{3}$$

where t is the CO_2 electrolysis time.

The half cell (cathodic) power conversion efficiency (PCE, assuming the overpotential of the oxygen evolution reaction is zero) of the formate products was calculated using:

$$PCE(\%) = \frac{(1.23 - E_{formate}) \times FE_{formate}}{1.23 - E} \tag{4}$$

where E is the applied potential vs RHE, $E_{formate}$ is thermodynamic potential (-0.02 V vs RHE) of CO_2RR to formate[57].

The production rate for formate was calculated using the following equation:

$$\text{Prodution rate} = \frac{Q \times FE_{formate}}{F \times 2 \times t \times S} \tag{5}$$

where Q is the total charge passed and S is the geometric area of the electrode (1 cm^2).

DFT calculations. The DFT calculations were performed by Vienna ab initio simulation package (VASP)[58] program with projector augmented wave (PAW)[59] method and the kinetic energy cut off was set to be 500 eV. The convergence criterion for electronic self-consistent iteration was set to be 10^{-4} eV. The atomic positions were fully relaxed until the force on each atom is less than 0.02 eV Å^{-1}. The Perdew−Burke−Ernzerhof[60] generalized gradient approximation exchange-correlation functional was used throughout. The slab model of In (101), In_2S_3 (311), and $ZnIn_2S_4$ (102) surface were constructed from the optimized In, In_2S_3, and $ZnIn_2S_4$ crystal structure. At the same time, a vacuum layer of 15 Å is established in the c-axis direction to ensure the separation between slabs. In addition, the surface formate species takes a unit negative charge, and, the present DFT calculation is not so great as to describe this kind of system carrying a neat charge. Thus, HCOOH was considered as the final product to describe this reaction rather than formate, in line with the DFT calculation in many researches[18,61,62]. The COHPs were computed using the developed lobster program[63–65].

Here, The Gibbs free energies were calculated at 25 °C and 1 atm:

$$\Delta G_{ads} = \Delta E_{ads} + \Delta ZPE - T\Delta S + eU \tag{6}$$

where ΔE_{ads}, ΔZPE, T, ΔS, U, and e are the binding energy, zero-point energies changes, temperature, entropy changes, applied potential at the electrode, and charge transferred, respectively.

Data availability

All experimental data within the article and its Supplementary Information are available from the corresponding author upon reasonable request.

References

1. Montoya, J. H. et al. Materials for solar fuels and chemicals. *Nat. Mater.* **16**, 70–81 (2017).
2. Mistry, H., Varela, A. S., Kühl, S., Strasser, P. & Cuenya, B. R. Nanostructured electrocatalysts with tunable activity and selectivity. *Nat. Rev. Mater.* **1**, 16009 (2016).
3. Gao, F.-Y. et al. High-curvature transition-metal chalcogenide nanostructures with a pronounced proximity effect enable fast and selective CO_2 electroreduction. *Angew. Chem. Int. Ed.* **59**, 8706–8712 (2020).
4. Fan, L., Xia, C., Zhu, P., Lu, Y. & Wang, H. Electrochemical CO_2 reduction to high-concentration pure formic acid solutions in an all-solid-state reactor. *Nat. Commun.* **11**, 3633 (2020).
5. Chen, Z. et al. Grain-boundary-rich copper for efficient solar-driven electrochemical CO_2 reduction to ethylene and ethanol. *J. Am. Chem. Soc.* **142**, 6878–6883 (2020).
6. Zhuang, T.-T. et al. Steering post-C–C coupling selectivity enables high efficiency electroreduction of carbon dioxide to multi-carbon alcohols. *Nat. Catal.* **1**, 421–428 (2018).
7. Niu, Z.-Z. et al. Hierarchical copper with inherent hydrophobicity mitigates electrode flooding for high-rate CO_2 electroreduction to multicarbon products. *J. Am. Chem. Soc.* **143**, 8011–8021 (2021).
8. Jiang, K. et al. Metal ion cycling of Cu foil for selective C–C coupling in electrochemical CO_2 reduction. *Nat. Catal.* **1**, 111–119 (2018).
9. Jouny, M., Luc, W. & Jiao, F. General techno-economic analysis of CO_2 electrolysis systems. *Ind. Eng. Chem. Res.* **57**, 2165–2177 (2018).
10. Bushuyev, O. S. et al. What should we make with CO_2 and how can we make it? *Joule* **2**, 825–832 (2018).
11. Hori, Y., Wakebe, H., Tsukamoto, T. & Koga, O. Electrocatalytic process of CO selectivity in electrochemical reduction of CO_2 at metal electrodes in aqueous media. *Electrochim. Acta* **39**, 1833–1839 (1994).
12. Ye, K. et al. In situ reconstruction of a hierarchical Sn−Cu/SnOx core/shell catalyst for high-performance CO_2 electroreduction. *Angew. Chem. Int. Ed.* **59**, 4814–4821 (2020).
13. Han, N. et al. Ultrathin bismuth nanosheets from in situ topotactic transformation for selective electrocatalytic CO_2 reduction to formate. *Nat. Commun.* **9**, 1320 (2018).
14. Wang, Z. et al. Exfoliated ultrathin $ZnIn_2S_4$ nanosheets with abundant zinc vacancies for enhanced CO_2 electroreduction to formate. *ChemSusChem* **14**, 852–859 (2020).
15. Zhou, J.-H. et al. Boosting electrochemical reduction of CO_2 at a low overpotential by amorphous Ag−Bi−S−O decorated Bi^0 nanocrystals. *Angew. Chem. Int. Ed.* **58**, 14197–14201 (2019).
16. Ma, W. et al. Promoting electrocatalytic CO_2 reduction to formate via sulfur-boosting water activation on indium surfaces. *Nat. Commun.* **10**, 892 (2019).
17. Grigioni, I. et al. CO_2 electroreduction to formate at a partial current density of 930 mA cm^{-2} with InP colloidal quantum dot derived catalysts. *ACS Energy Lett.* **6**, 79–84 (2020).
18. Zheng, X. et al. Sulfur-modulated tin sites enable highly selective electrochemical reduction of CO_2 to formate. *Joule* **1**, 794–805 (2017).
19. Yang, J. et al. Bi-based metal-organic framework derived leafy bismuth nanosheets for carbon dioxide electroreduction. *Adv. Energy Mater.* **10**, 2001709 (2020).
20. Gong, Q. et al. Structural defects on converted bismuth oxide nanotubes enable highly active electrocatalysis of carbon dioxide reduction. *Nat. Commun.* **10**, 2807 (2019).
21. Cao, C. et al. Metal-organic layers leading to atomically thin bismuthene for efficient carbon dioxide electroreduction to liquid fuel. *Angew. Chem. Int. Ed.* **59**, 15014–15020 (2020).
22. Wu, J., Sun, S.-G. & Zhou, X.-D. Origin of the performance degradation and implementation of stable tin electrodes for the conversion of CO_2 to fuels. *Nano Energy* **27**, 225–229 (2016).
23. Shi, Y. et al. Unveiling hydrocerussite as an electrochemically stable active phase for efficient carbon dioxide electroreduction to formate. *Nat. Commun.* **11**, 3415 (2020).
24. Cheng, H. et al. Surface nitrogen-injection engineering for high formation rate of CO_2 reduction to formate. *Nano Lett.* **20**, 6097–6103 (2020).
25. Huang, Z.-F. et al. Hollow cobalt-based bimetallic sulfide polyhedra for efficient all-pH-value electrochemical and photocatalytic hydrogen evolution. *J. Am. Chem. Soc.* **138**, 1359–1365 (2016).
26. Chai, B., Peng, T., Zeng, P., Zhang, X. & Liu, X. Template-free hydrothermal synthesis of $ZnIn_2S_4$ floriated microsphere as an efficient photocatalyst for H_2 production under visible-light irradiation. *J. Phys. Chem. C* **115**, 6149–6155 (2011).

27. Chen, Z. et al. Photocatalytic degradation of dyes by $ZnIn_2S_4$ microspheres under visible light irradiation. *J. Phys. Chem. C.* **113**, 4433–4440 (2009).

28. Gou, X. et al. Shape-controlled synthesis of ternary chalcogenide $ZnIn_2S_4$ and $CuIn(S,Se)_2$ nano-/microstructures via facile solution route. *J. Am. Chem. Soc.* **128**, 7222–7229 (2006).

29. Otsuka, R., Seo, W. S. & Koumoto, K. Thermoelectric properties of layer-structured $(ZnS)_mIn_2S_3$. *Key Eng. Mater.* **181–182**, 59–62 (2000).

30. Aymerich, F., Meloni, F. & Mula, G. Electron band structure of α-$ZnIn_2S_4$ and related polytypes. *Solid State Commun.* **29**, 235–238 (1979).

31. Fu, X. et al. Photocatalytic performance of tetragonal and cubic β-In_2S_3 for the water splitting under visible light irradiation. *Appl. Catal. B* **95**, 393–399 (2010).

32. Ma, W. et al. Monoclinic Scheelite Bismuth Vanadate derived Bismuthene nanosheets with rapid kinetics for electrochemically reducing carbon dioxide to formate. *Adv. Funct. Mater.* **31**, 2006704 (2021).

33. García de Arquer, F. P. et al. 2D metal oxyhalide-derived catalysts for efficient CO_2 electroreduction. *Adv. Mater.* **30**, 1802858 (2018).

34. Xing, Y. et al. Bi@Sn core–shell structure with compressive strain boosts the electroreduction of CO_2 into formic acid. *Adv. Sci.* **7**, 1902989 (2020).

35. Liang, C. et al. High efficiency electrochemical reduction of CO_2 beyond the two-electron transfer pathway on grain boundary rich ultra-small SnO_2 nanoparticles. *J. Mater. Chem. A* **6**, 10313–10319 (2018).

36. Shang, H. et al. Design of a single-atom indium$^{\delta+}$-N_4 interface for efficient electroreduction of CO_2 to formate. *Angew. Chem. Int. Ed.* **59**, 22465–22469 (2020).

37. Kwon, I. S. et al. Selective electrochemical reduction of carbon dioxide to formic acid using indium–zinc bimetallic nanocrystals. *J. Mater. Chem. A* **7**, 22879–22883 (2019).

38. Zhang, X. et al. Defects and conductive nitrogen−carbon framework regulated ZnInOx nanosheets for boosting CO_2 electrocatalytic reduction. *Appl. Catal. B* **279**, 119383 (2020).

39. Luo, W., Xie, W., Li, M., Zhang, J. & Züttel, A. 3D hierarchical porous indium catalyst for highly efficient electroreduction of CO_2. *J. Mater. Chem. A* **7**, 4505–4515 (2019).

40. Zhang, A. et al. Harmonizing the electronic structures of the adsorbate and catalysts for efficient CO_2 reduction. *Nano Lett.* **19**, 6547–6553 (2019).

41. Wang, J. et al. Heterostructured intermetallic CuSn catalysts: high performance towards the electrochemical reduction of CO_2 to formate. *J. Mater. Chem. A* **7**, 27514–27521 (2019).

42. Zhang, A. et al. Nickel doping in atomically thin tin disulfide nanosheets enables highly efficient CO_2 reduction. *Angew. Chem. Int. Ed.* **57**, 10954–10958 (2018).

43. Yuan, X. et al. Decoration of In nanoparticles on In_2S_3 nanosheets enables efficient electrochemical reduction of CO_2. *Chem. Commun.* **56**, 4212–4215 (2020).

44. Shen, S., Chen, J., Wang, X., Zhao, L. & Guo, L. Microwave-assisted hydrothermal synthesis of transition-metal doped $ZnIn_2S_4$ and its photocatalytic activity for hydrogen evolution under visible light. *J. Power Sources* **196**, 10112–10119 (2011).

45. Lopez-Rivera, S. A., Martinez, L., Fontal, B., Giriat, W. & Medina, F. Raman study of a $ZnIn_2S_4$ layered compound. *Semicond. Sci. Technol.* **10**, 645–652 (1995).

46. Tao, H., Mao, S., Dong, G., Xiao, H. & Zhao, X. Raman scattering studies of the Ge–In sulfide glasses. *Solid State Commun.* **137**, 408–412 (2006).

47. RRUFFTM Project https://rruff.info/Indium.

48. Wu, Y. et al. Converting copper sulfide to copper with surface sulfur for electrocatalytic alkyne semi-hydrogenation with water. *Nat. Commun.* **12**, 3881 (2021).

49. Hu, C. et al. In situ electrochemical production of ultrathin nickel nanosheets for hydrogen evolution electrocatalysis. *Chem* **3**, 122–133 (2017).

50. Luc, W. et al. SO_2 induced selectivity change in CO_2 electroreduction. *J. Am. Chem. Soc.* **141**, 9902–9909 (2019).

51. Liu, D., Liu, Y. & Li, M. Understanding how atomic sulfur controls the selectivity of the electroreduction of CO_2 to formic acid on metallic Cu surfaces. *J. Phys. Chem. C.* **124**, 6145–6153 (2020).

52. Aymerich, F., Meloni, F. & Mula, G. Electronic properties of the layer compound $ZnIn_2S_4$. *Phys. B+C.* **99**, 314–317 (1980).

53. Tao, W. et al. Electronic structure and oxidation mechanism of nickel–copper converter matte from first-principles calculations. *ACS Omega* **5**, 20090–20099 (2020).

54. Wei, T.-R. et al. Exceptional plasticity in the bulk single-crystalline van der Waals semiconductor InSe. *Science* **369**, 542–545 (2020).

55. Hao, Y.-C. et al. Promoting nitrogen electroreduction to ammonia with bismuth nanocrystals and potassium cations in water. *Nat. Catal.* **2**, 448–456 (2019).

56. Ma, M., Kim, S., Chorkendorff, I. & Seger, B. Role of ion-selective membranes in the carbon balance for CO_2 electroreduction via gas diffusion electrode reactor designs. *Chem. Sci.* **11**, 8854–8861 (2020).

57. Kuhl, K. P., Cave, E. R., Abram, D. N. & Jaramillo, T. F. New insights into the electrochemical reduction of carbon dioxide on metallic copper surfaces. *Energy Environ. Sci.* **5**, 7050–7059 (2012).

58. Kresse, G. & Hafner, J. Ab initio molecular dynamics for liquid metals. *Phys. Rev. B* **47**, 558–561 (1993).

59. Blöchl, P. E. Projector augmented-wave method. *Phys. Rev. B* **50**, 17953–17979 (1994).

60. Perdew, J. P., Burke, K. & Ernzerhof, M. Generalized gradient approximation made simple. *Phys. Rev. Lett.* **77**, 3865–3868 (1996).

61. Yoo, J. S., Christensen, R., Vegge, T., Nørskov, J. K. & Studt, F. Theoretical insight into the trends that guide the electrochemical reduction of carbon dioxide to formic acid. *ChemSusChem* **9**, 358–363 (2016).

62. Jiang, B., Zhang, X.-G., Jiang, K., Wu, D.-Y. & Cai, W.-B. Boosting formate production in electrocatalytic CO_2 reduction over wide potential window on Pd surfaces. *J. Am. Chem. Soc.* **140**, 2880–2889 (2018).

63. Maintz, S., Deringer, V. L., Tchougréeff, A. L. & Dronskowski, R. LOBSTER: a tool to extract chemical bonding from plane-wave based DFT. *J. Comput. Chem.* **37**, 1030–1035 (2016).

64. Dronskowski, R. & Bloechl, P. E. Crystal orbital Hamilton populations (COHP): energy-resolved visualization of chemical bonding in solids based on density-functional calculations. *J. Phys. Chem.* **97**, 8617–8624 (1993).

65. Deringer, V. L., Tchougréeff, A. L. & Dronskowski, R. Crystal orbital Hamilton population (COHP) analysis as projected from plane-wave basis sets. *J. Phys. Chem. A* **115**, 5461–5466 (2011).

Acknowledgements

Author contributions

M.R.G. and K.B.T. conceived and supervised the project. L.P.C. performed the experiments, collected and analyzed the data. Z.Z.N. helped with the test and analysis of NMR. X.L.Z. carried out the DFT calculations. P.P.Y., J.L., F.Y.G., and Z.Z.W. helped with electrochemical data collection and analysis. M.R.G., K.B.T., and L.P.C. co-wrote the paper. All authors discussed the results and commented on the paper.

Competing interests

The authors declare no competing interests.

Additional information